J. Eur. Opt. Society-Rapid Publ. 2023, **19**, 23

https://doi.org/10.1051/jeos/2023018
Available online at: https://jeos.edpsciences.org

Journal of the European Optical Society-Rapid Publications

Special Issue - EOSAM 2022
Guest editors: Patricia Segonds, Gilles Pauliat and Emiliano Descrovi

RESEARCH ARTICLE OPEN ACCESS

Application of imaging ellipsometry and white light interference microscopy for detection of defects in epitaxially grown 4H–SiC layers

Elena Ermilova*, Matthias Weise, and Andreas Hertwig

Bundesanstalt für Materialforschung und -prüfung (BAM), Division 6.1 Surface Analysis and Interfacial Chemistry, Unter den Eichen 44–46, D-12203 Berlin, Germany

Received 31 January 2023 / Accepted 5 April 2023

Abstract. Critical defects, also known as device killers, in wide bandgap semiconductors significantly affect the performance of power electronic devices. We used the methods imaging ellipsometry (IE) and white light interference microscopy (WLIM) in a hybrid optical metrology study for fast and non-destructive detection, classification, and characterisation of defects in 4H–SiC homoepitaxial layers on 4H–SiC substrates. Ellipsometry measurement results are confirmed by WLIM. They can be successfully applied for wafer characterisation already during production of SiC epilayers and for subsequent industrial quality control.

Keywords: Imaging ellipsometry, White light interference microscopy, 4H–SiC, Defects.

1 Introduction

Increasing energy demand and climate change require the development and effective application of reliable and cost-effective power electronics. Silicon carbide (SiC) belongs to wide bandgap (WBG) semiconductors and due to its outstanding properties is one of the most promising materials for next generation power electronics. SiC has high thermal conductivity, which is also common with other WBG materials. SiC-based devices can be employed at higher voltages and higher frequencies compared with silicon-based solutions [1, 2]. SiC is found to have high potential for various applications like automotive or smart grids.

High-quality SiC epitaxial wafers are needed to ensure the high yield and long-term reliability of power electronic devices. However, some types of defects on SiC substrates or in the homoepitaxial SiC layers, e.g., the so-called "triangles" or "carrots" (also known as "killer defects"), can significantly affect the performance of electronic devices [2–4]. The accurate detection and characterisation of defects and the determination of defect densities is of key importance in the electronic device industry. Apart from causing costs for broken part replacement, undetected defects are a source of energy inefficiency and a potential hazard for human life and health, and for the environment.

To effectively exploit SiC power devices, we need to understand mechanisms of defect formation and device failure. Different types of defects have different probabilities of disabling devices, resulting in different impact on device performance [5, 6]. Besides detection and classifications, reduction of defect density is a key task for semiconductor industry. It is of great importance to maintain low defect density at transitions to large diameter wafers.

4H–SiC is a most used polytype for power electronics devices. Different morphologies of triangular defects on 4H–SiC epitaxial wafers are known [7]. Substrate defects like scratches are thought to cause triangular defects or step bunching on the epitaxial 4H–SiC wafers. Additionally, downfall particles of different sizes can disturb homoepitaxial step-flow and lead to formation of this type of defects. The spherical part and the triangular pit can be recognized within the defect. In the pit, facetted structures can be generated during the epitaxy flow. It was found that these structures contain the cubic 3C–SiC crystal inclusions, which could be partly or completely overgrown by 4H–SiC polytype [7].

Different surface and subsurface characterisation methods have been applied to detect and characterize the SiC defects: electron microscopy, atomic force microscopy, photoluminescence, X-ray topography, defect-selective etching, Raman spectroscopy, cathodoluminescence, optical coherence tomography, optical microscopy, etc. [4–9]. The review article of Chen et al. [6] provides a very detailed overview of the above-mentioned methods and summarizes the advantages and disadvantages of these methods when used for investigation of different types of the defects in SiC.

* Corresponding author: elena.ermilova@bam.de

Table 1. Comparison of the imaging ellipsometry and the white light interference microscopy techniques.

	Imaging ellipsometry	White light interference microscopy
Sample preparation	None	None
Non-destructive	Yes	Yes
Scanning	Yes	Yes
Measurement of optical/dielectric properties	Yes	Yes
Topography investigation	No	Yes
Angle of incidence*	Variable	Normal incidence
	38°–90°	0°
Lateral imaging resolution for used experimental setups (50× objectives)*	1 µm	< 1 µm
Measurement time*	seconds to minutes	seconds

* Values are given for Nanofilm_EP4 imaging ellipsometer (Accurion) and Zygo NexView white light interference microscope.

For effective in-line quality control fast and non-destructive methods are required. The goal of this study is development of hybrid measurement method consisting of several techniques, which allows to detect, classify, and analyse critical defects, also known as device killers. In this publication we demonstrate how optical methods such as imaging ellipsometry and white light interference microscopy (WLIM) can be applied for investigation of triangle defects in epitaxially grown 4H–SiC layers on 4H–SiC substrates.

Ellipsometry is known to have a very high sensitivity to the surface and interface structures whereby the measured ellipsometric transfer quantities can be considered as a fingerprint of materials. Model-based analysis of the measured data allows for determination of optical/dielectric properties of materials [10]. Due to its polarization sensitivity, imaging ellipsometry provides enhanced contrast for defect detection of transparent homoepitaxial 4H–SiC layers on the transparent 4H–SiC substrates compared to the optical microscopy. We demonstrate the capability of imaging ellipsometry to visualize the defects and determine the changes in ellipsometric transfer quantities over the sample surface in the field of view of the experimental setup. Such changes indicate the changes in the sample structure even if they are not properly resolved by experimental setup.

WLIM measurements can be considered as a complementary metrology technique. It allows to examine the defect topography and contribute to understanding of defect formation and propagation mechanisms. Knowledge of defect morphology helps to understand the impact of critical defects on electronic device performance.

Table 1 gives a brief overview of the techniques used in this study. The lateral resolution of the experimental setups is determined by the measurement wavelength, the numerical aperture of the optics and the pixel size of the detectors. It can achieve 1 µm for Nanofilm_EP4 imaging ellipsometer (Accurion) and is better than 1 µm for Zygo NexView white light interference microscope when using 50× objectives.

Vertical scan over the sample surface by WLIM topography measurements takes a few seconds. The entire surface in the field of view is scanned simultaneously. To acquire the focused images and the maps of ellipsometric transfer quantities by imaging ellipsometer, the focus scan from the top to the bottom of the image in the field of view is carried out. The acquisition time of the ellipsometric scanned images is comparable to the measurement time of the WLIM. The acquisition time of the focused maps can take several seconds to a few minutes.

The 12 µm 4H–SiC homo-epitaxial layers on 4H–SiC substrates for this study were provided by Aixtron. 4° off-cut substrates were nitrogen doped (n+) with doping concentration of $1.00 \pm 0.03 \times 10^{16}$ cm^{-3}. The 10 × 10 mm samples with the thickness of 0.5 mm were double-sided polished.

2 Imaging ellipsometry measurements of 4H–SiC epitaxial layers

Ellipsometry is a phase-sensitive method which allows to characterize thin transparent and semi-transparent layers in the range from sub-nm to tens of µm in a broad spectral range. Ellipsometry measures changes in polarization when light is reflected from the sample's surface at oblique angles of incidence (AOI) [10, 11]. The ratio of the complex reflection coefficients $\tilde{r}_p$ and $\tilde{r}_s$ for p- and s-polarized light is measured during the experiment (see Eq. (1)).

$$\rho = \frac{\tilde{r}_p}{\tilde{r}_s} = \tan \Psi e^{-i\Delta}. \quad (1)$$

Ψ corresponds to the ratio of the amplitudes of p- and s-polarized light, whereas Δ corresponds to the phase differences between p- and s-polarized waves after reflection from the surface. The obtained ellipsometric transfer quantities Ψ and Δ represent material fingerprints. To determine the thickness of thin layers as well as optical/dielectric properties of layer materials a model-based fitting procedure is applied [10, 11]. Sample roughness, composition, uniformity (thickness inhomogeneity, refractive index gradient) of the layers can be determined from the fit [12, 13]. It is worth to emphasize, that Muller matrix ellipsometry allows extensive analysis of optically anisotropic samples.

Imaging ellipsometry combines the ellipsometry and optical microscopy techniques. It stands out due to polarization sensitivity and very high contrast for surface structures [14–16]. Surface structures with very low refractive index contrast could be clearly visualized. In the ellipsometry experiment light reflected from the sample surface passes through the objective lenses and is detected by a CCD camera in the imaging ellipsometry setup. The ellipsometric transfer quantities Ψ and Δ are measured for individual camera pixel. Thus, the spatially resolved maps of ellipsometric transfer quantities can be acquired. The measured Ψ and Δ values depend on the complex refractive index of the substrate and the layers, the layer thickness, the wavelength, and the angle of incidence of the probing light. Accordingly, by adjusting the wavelength and the angle of incidence, the optimal conditions can be found to acquire the maps of ellipsometric transfer quantities with high contrast and high spatial resolution. In contrast to the conventional spectroscopic ellipsometer, imaging ellipsometer provides the possibility to extract the ellipsometric transfer quantities for selected region of interest (ROI) within the field of view.

Ellipsometric measurements were performed using Nanofilm_EP4 imaging ellipsometer (Accurion). Measurement data were acquired in RCE (rotating compensator ellipsometry) mode. Imaging ellipsometry setup is shown schematically in Figure 1.

In RCE mode polarizer (P) and analyzer (A) azimuths are fixed at +45° (in two-zone mode $A = \pm 45°$). Ellipsometric transfer quantities Ψ and Δ are determined from measured Fourier coefficients of detected light intensities when the compensator (C) rotates by 180°.

Ellipsometry has been widely used to study semiconductor materials and SiC in particular [17–19]. SiC is transparent in a visible spectral range below the bandgap. Thus, the partly polarized reflections from the backside of the thin SiC substrate can reach the detector and affect the measured ellipsometric quantities Ψ and Δ [20]. To eliminate the backside reflections, we apply the knife edge illumination method of Nanofilm_EP4 imaging ellipsometer [14].

According to the operating principle shown in Figure 2 the part of the incident light is screened, and the backside reflections are eliminated for the certain sample area in the field of view. This area is marked with the purple arrows.

Figure 3 shows the ellipsometric microscope image (a), and Ψ – and Δ – maps ((b) and (c), respectively) of a triangular defect on 12 µm 4H–SiC epilayer grown on 4H–SiC substrates. The image was taken using a 20× objective at the wavelength $\lambda = 550$ nm and the angle of incidence AOI = 45°. This angle was chosen for better image quality due to less focus scanning range required. The choice of this wavelength was due to highest light source intensity and therefore best inherent contrast of the instrument. The azimuths of the polarizer (P), analyzer (A) and compensator (C) were respectively $P = 45°$, $A = 45°$, $C = 142°$. The dark part on the top of Figure 3a corresponds to the region with no reflected light (because the beam cutter is used). On the ellipsometric image and Ψ –map in Figures 3a–3b, the spherical part of the defect is visible.

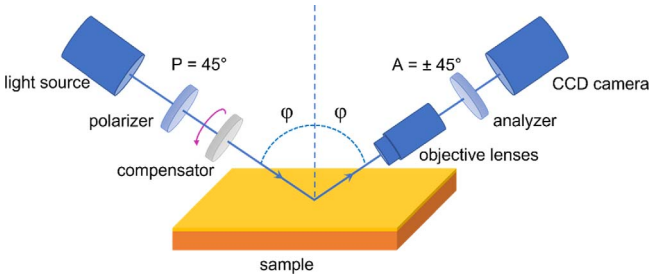

Fig. 1. Schematical representation of imaging ellipsometry setup operating in RCE mode. φ is the angle of incidence.

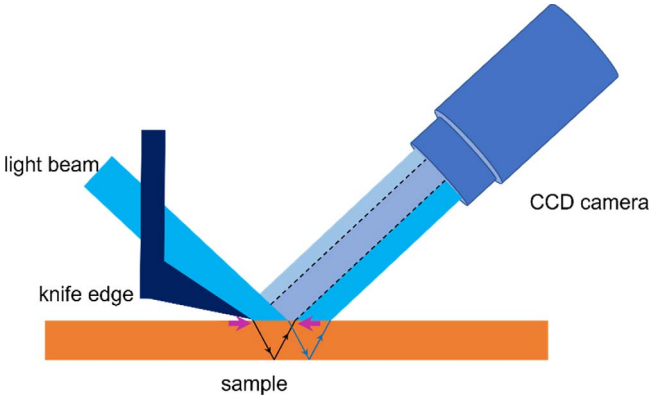

Fig. 2. Schematical representation of knife edge illumination method (Accurion) using the example of the double-sided polished transparent substrate. The sample area marked with the purple arrows is free of the backside reflections.

This is the double image of the defect caused by the reflection from the backside of the substrate. The knife edge illumination method therefore allows to eliminate the incoherent backsides reflections that affect the measured ellipsometric transfer quantities and to avoid the double detection of the same defects. The brighter part on the bottom contents the light reflected from the back side of the transparent substrate. The part in the middle is free from backside reflections. The maps were acquired at the wavelength $\lambda = 555$ nm. To acquire both the image and the monocromatic maps, the focus scan from the top to the bottom of the image in the field of view is performed.

The spherical area and triangle pit of a defect can be clearly detected. The spherical area is reported to be caused by impacts of particles before or during the epitaxy process [4]. It disturbs the epitaxial growth and can lead to formation of triangle pits. We can clearly distinguish the smaller triangle region at the apex inside the main triangular pit. Inside the triangular pit we can also see the lines with lower contrast which form an inner triangle. A step at the end of the right part of the pit is visible and clearly resolved on the ellipsometric maps in Figure 3.

Using the Accurion software one can analyse line profiles of Ψ and Δ pixel values. The line in Figures 3b and 3c pass through the triangle of a smaller size on the apex of

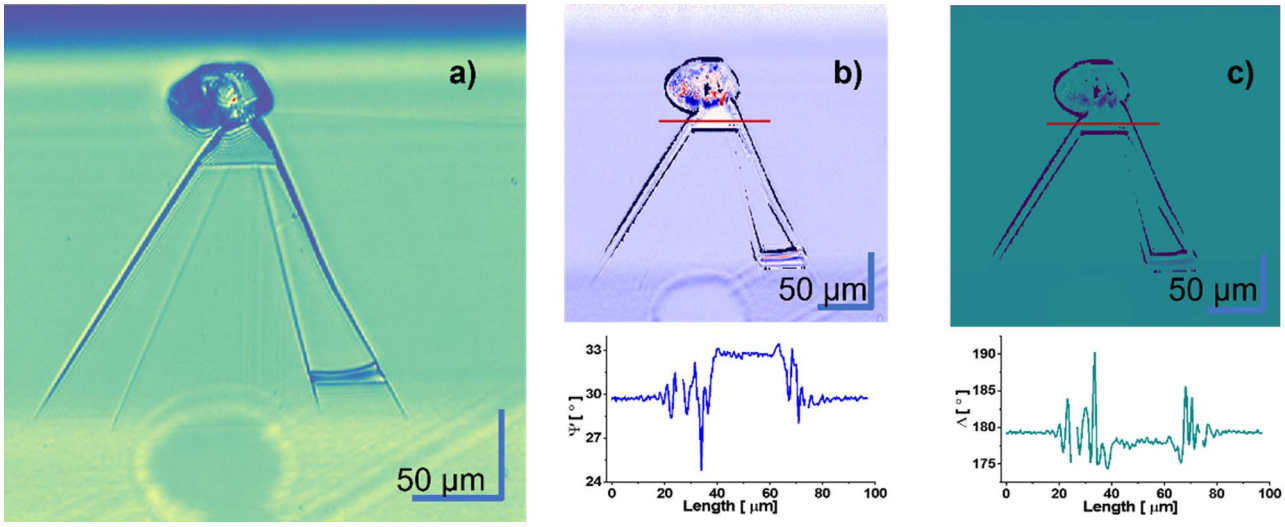

Fig. 3. a) Ellipsometric microscope image, b) Ψ-map with selected line profile and c) Δ-map with selected line profile of a triangular defect on 12 µm 4H–SiC epilayer grown on 4H–SiC substrate.

the triangular pit. Significant variations of Ψ and Δ values are obtained at the edges and inside the smaller triangular region compared with the defect free area. Since ellipsometry has a high sensitivity to the surface and interface structures, these changes can demonstrate the modified material structure or inhomogeneity of sample dielectric properties. Line profiles of measured Ψ and Δ at certain wavelengths and angles of incidence enable first conclusions about the structure of different defect areas. Despite high spatial resolution and high polarisation sensitivity of imaging ellipsometric technique, the topography of this defect part is not entirely clear from the ellipsometric measurements.

Figure 4 shows Ψ and Δ histograms over the certain regions of interest (ROIs 0, 1, 2). The ROI-0 is selected in a small triangle at the apex of the main triangular pit, ROI-1 – outside the defect and ROI-2 inside the triangle pit. The entire Ψ- and Δ-ranges within the measured regions are divided into the certain number of equal intervals. The relative frequencies for each value are plotted in the histograms. Histogram analysis shows that Ψ – range in the ROI-0 is broader compared to that of ROI-1 and -2 Figure 4a. Ψ-distributions for ROI-1 outside and ROI-2 inside the pit overlap. The histogram centre for the ROI-2 inside the defect is slightly shifted to the lower Ψ-values compared to the ROI-1 outside the defect area. The histogram centre for the ROI-0 is located at significantly higher Ψ-values. Centre positions of Ψ histograms for ROI-0 and ROI-1 differ by approximately 3°.

Figure 4b shows the broad distribution of Δ-values for the ROI-0 compared to the sharp peaks of Δ-values in ROI-1 and ROI-2. The dispersion maximum for ROI-0 is shifted to the lower Δ-values. Variation in Δ values for the ROI-0 is bigger than 4°. The distribution of Δ for ROI-2 is shifted compared to the values for ROI-1. According to Figures 4a and 4b the Ψ- and Δ-distributions for ROI-0 is broader than those of ROI-1 and ROI-2. That means that the probing light in ROI-0 sees the modified surface conditions compared to the regions outside the defect. This finding is in very good agreement with the line profiles discussed earlier.

Histogram is a very informative analysis tool which could bring into light surface structures which are not resolved by imaging ellipsometry. However, it should be noted that the dark edges of the defect on the maps correspond to very low detected light intensities. This could be explained by steep structures in the defect which are not visible on the ellipsometric images. To clarify the topography of the triangle defect, additional investigations by means of coherence scanning white light interference microscope were performed.

3 Coherence scanning white light interferometry measurements of 4H–SiC epitaxial layers

Coherence scanning white light interference microscopy (WLIM) is a non-contact technique that operates at normal incidence and scans the surface in vertical direction to determine surface topography, height, and shape of surface structures [21]. Light beam from the broadband light source is divided into the measurement beam and the reference beam. The measurement light reflected from the sample surface is recombined with the reference light reflected from the reference surface. The superimposed beams are passed on to the camera and form the interference signal. Because of low coherence of the white light source, the white light interference patterns are localized in space. Height differences on the sample result in differences in location of interference patterns [21, 22]. Location points are calculated for each camera pixel during the scan and topography image is created. The highest point on the interference pattern envelope corresponds to the focus position of the objective. The sample surface in the field

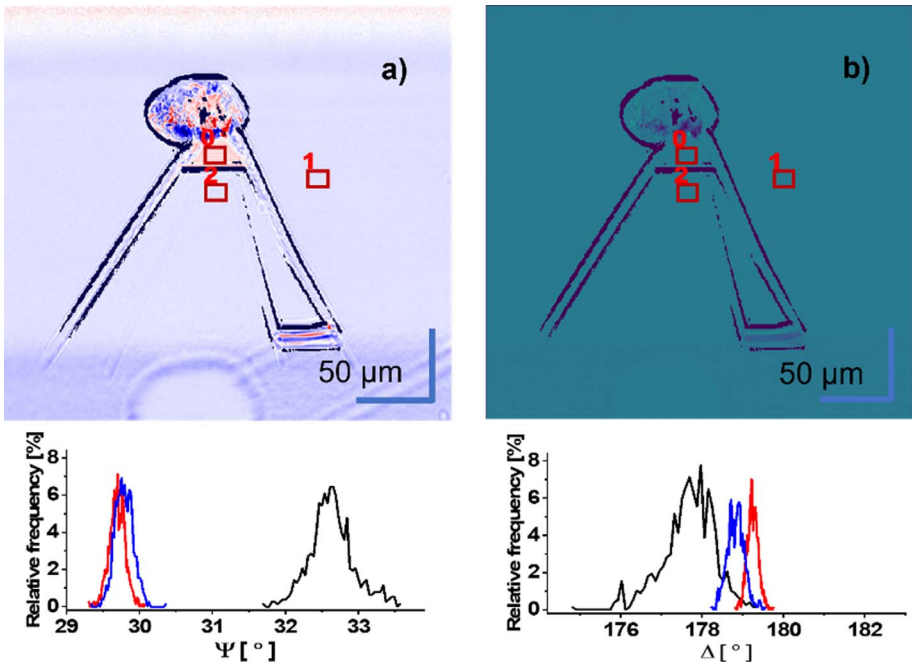

Fig. 4. a) Ψ-map with the histogram of Ψ values and b) Δ-map with the histogram of Δ values over the ROIs (black – ROI-0, red – ROI-1, blue – ROI-2) at $\lambda = 550$ nm and AOI = 45°.

of view of white light interference microscope is examined in a single measurement.

Sample measurements were carried out with the microscope Zygo NexView with a 20× (Figs. 5 and 6a) and 100× Mirau-objectives (Fig. 6b). Vertical resolution for WLIM measurements is in the range of 1 nm [23], spatial resolutions are ~0.7 µm for 20× and ~0.4 µm for 100× objectives.

Figure 5 shows the two-dimensional WLIM images with the height profiles. The horizontal axis corresponds to the distances on the sample surface along the profile lines. The vertical axis indicates the height at corresponding points along the profile lines. The profile in Figure 5a passes along the right side (on ellipsometric image in Fig. 3) of the triangular pit (in the Fig. 5 – the lower part) through the step (blue according to the WLIM color scale) towards the spherical part, the "head", of the defect and ends in the smaller triangular region at the apex of the pit. The smaller triangle region, as well as a step (blue in Fig. 5a) are clearly resolved by means of imaging ellipsometry (Figs. 3 and 4). According to the height profile the step goes 600 nm down into the layer. This was not clear from the ellipsometric images. The profile also shows the flat slope of the triangular pit. It becomes very steep in the vicinity of the spherical part of the defect. At the endpoint of the profile near the head of the defect, it is deeper than 1 µm, see Figures 5a and 6a.

Figure 5b shows the profile across the triangular pit of a defect. It is evident that the triangular defect area forms the pit with the depth of more than 100 nm. The inner part of triangular region is obtained to build the steep steps with the outer areas. The step height was measured to be around 10 nm for the upper part and around 40 nm for the lower part of the triangular pit. These findings are consistent with the ellipsometric image in Figure 3a which shows a triangle with the sides with the low contrast compared to the outer triangular pit. A shallow groove above and below the defect is visible in Figures 5a–5c as well as in Figure 6a. The width of the groove is comparable to the size of the defect, and it was found to extend far beyond the actual defect, in some cases to the edges of the samples. The step height of the groove reaches 6 nm as seen in Figure 5c. There is some indication that this groove can be made visible by imaging ellipsometry and the possibility of measuring it accurately by this method is currently under investigation.

Figure 6b shows a three-dimensional WLIM image of the spherical part of the defect. The line profile below shows that that the spherical head extends several µm above the layer surface (Fig. 6b). It has a step-like structure, that may be expected for the case than a particle lands on the surface before or during the epitaxy process and is overgrown. At the edge of the head, a narrow dip is observed with a depth of more than 2 µm relative to the defect free sample surface (Fig. 6b). The overall topography around the triangle defect, especially the dip around the head and at the apex of the triangle pit indicate that the epitaxial flow was disturbed by the presence of the particle on the substrate surface.

WLIM results are consistent with the ellipsometry maps where dark defect edges are obtained on the spatially resolved maps. SiC is transparent in the visible range below the bandgap and the steep steps at the edges and in the middle of a triangle, around a "head" and at the apex of the pit prevent detection of the light intensity during the ellipsometry measurements at oblique angles of incidence.

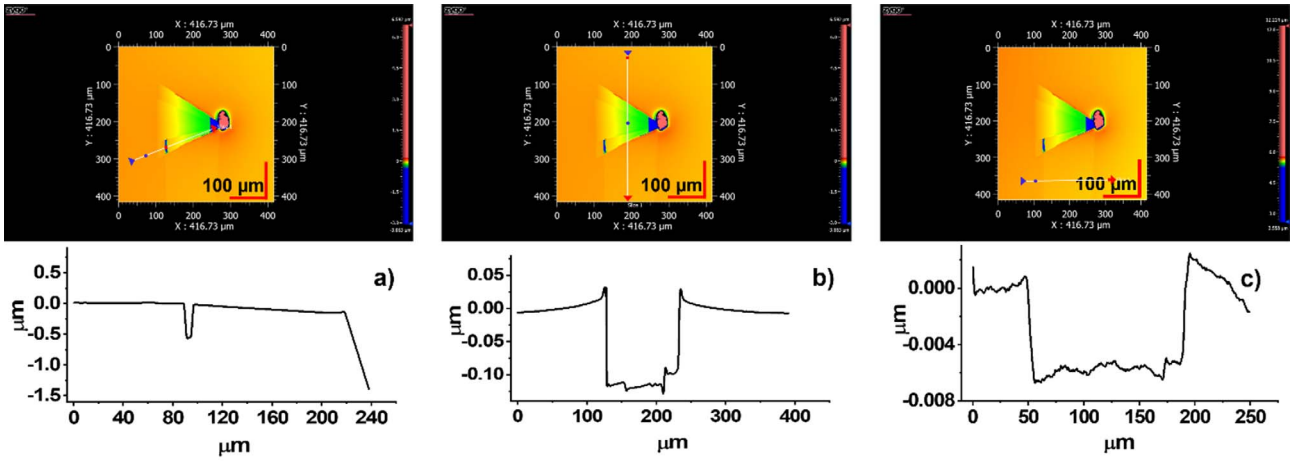

Fig. 5. WLIM image and surface profiles of a triangular defect on 12 µm 4H–SiC epilayer grown on 4H–SiC substrate.

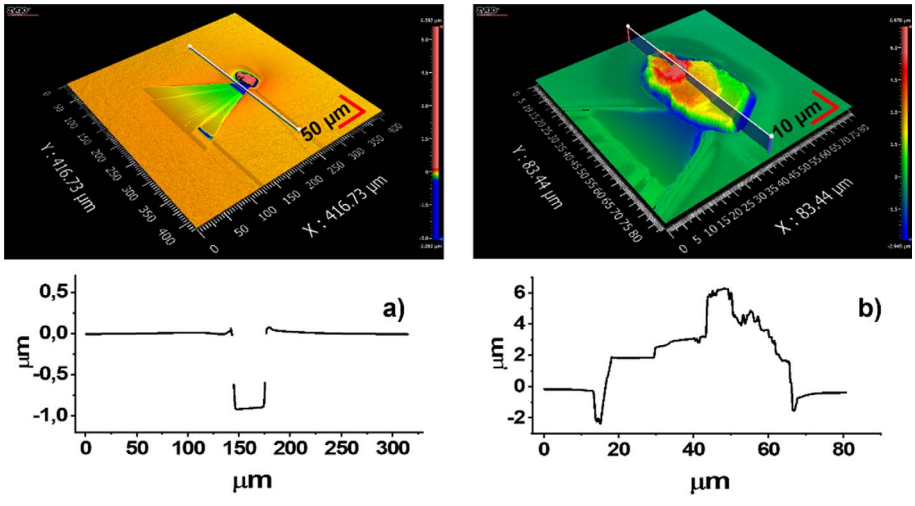

Fig. 6. WLIM 3D-images of a) the entire defect and b) the spherical area of defect on 12 µm 4H–SiC epilayer grown on 4H–SiC substrate.

WLIM experiments can clarify the topography of the defects, confirm the ellipsometry measurement results and explain the surface structures which are not visible by imaging ellipsometry.

Such hybrid optical metrology method as WLIM and imaging ellipsometry can be used to better understand the mechanism of the development of the defects as well as their effects on the material's optoelectronic properties.

4 Conclusion

We have shown that hybrid measurement technique using spectroscopic and imaging ellipsometry as well as white light interference microscopy enables fast and non-destructive detection and traceable characterization of "killer" defects in epitaxially grown 4H–SiC layers.

Imaging ellipsometry provides enhanced contrast to the surface structures for transparent, anisotropic SiC samples. Elimination of back side reflections by means of knife edge illumination avoids time-consuming and destructive roughening of the samples. Quantitative analysis of the spatially resolved maps of ellipsometric transfer quantities allows to detect and classify critical defects on 4H–SiC homoepitaxial wafers. For determination of the ordinary and extraordinary dielectric functions of optically anisotropic 4H–SiC, additional measurements on the samples with different crystal surface orientation as well as complex fitting procedure are required. These are difficult to implement in the in-line control during the manufacture of SiC wafers and power electronic devices. Modelling of the measured parameters would be the next step in our study to investigate the effect of defects on the material's optoelectronic properties.

WLIM topography measurements clarify the surface topography and explore the accurate geometrical features of the surface structures in the 4H–SiC epilayer, which cannot be directly determined by means of imaging

ellipsometry. Due to its high vertical resolution, scanning WLIM provides detailed information about the morphology of defects and contributes to understanding of formation mechanisms and propagation of defects in epitaxial 4H–SiC layers. It helps to reduce defect density already during production process and achieve the high quality of epitaxial layers. Due to the low measurement times and stitching options of the instruments, both methods can be effectively implemented for full wafer characterization to classify the defects and determine defect densities.

Both measurement methods are proven to work in a quality management environment as they are operated in laboratories accredited according to DIN EN ISO/IEC 17025 [24]. Therefore, ellipsometry and white light interference microscopy are very promising candidates for use as production monitoring tools for SiC epilayers and for subsequent industrial quality control. In the future, we expect that analysis methods will be able to detect and characterise defects within one measurement only – at least to the extent required to monitor production. This is still not possible for many production relevant samples as complex layer stacks – or modified materials due to defects – are often too complex to be modelled with easy models. For the moment, hybrid approaches to this issue are still the best compromise. These involve several methods and use fingerprinting rather than modelling of ellipsometric data.

Conflict of interest

The authors declare no conflict of interest.

Acknowledgments. Authors thank AIXTRON for providing samples for the PowerElec project. The PowerElec project has received funding from the EMPIR programme co-funded by the Participating States and from European Union's Horizon 2020 research and innovation programme under JRP 20IND09.

References

1 Langpoklakpam C., Liu A.-C., Chu K.-H., Hsu L.-H., Lee W.-C., Chen S.-C., Sun C.-W., Shih M.-H., Lee K.-Y., Kuo H.-C. (2022) Review of silicon carbide processing for power MOSFET, *Crystals* **12**, 2, 245.
2 Wellmann P., Ohtani N., Rupp R. (2022) *Wide bandgap semiconductors for power electronics: Materials, devices, applications*, Wiley.
3 Fraga M.A., Bosi M., Negri M. (2015) Silicon carbide in microsystem technology – thin film versus bulk material, in: *Advanced Silicon Carbide Devices and Processing*, Sep 17, 2015, InTech. https://doi.org/10.5772/60970.
4 Dong L., Sun G.S., Yu J., Yan G.G., Zhao W.S., Wang L., Zhang X.H., Li X.G., Wang Z.G. (2014) Structure and Origin of Carrot Defects on 4H-SiC Homoepitaxial Layers, *Mater. Sci. Forum* **778–780**, 354–357.
5 Matsuhata H., Sugiyama N., Chen B., Yamashita T., Hatakeyama T., Sekiguchi T. (2016) Surface defects generated by intrinsic origins on 4H-SiC epitaxial wafers observed by scanning electron microscopy, *Microscopy* **66**, 2, 95–102.
6 Chen P.-C., Miao W.-C., Ahmed T., Pan Y.-Y., Lin C.-L., Chen S.-C., Kuo H.-C., Tsui B.-Y., Lien D.-H. (2022) Defect inspection techniques in SiC, *Nanoscale Res. Lett.* **17**, 1, 30.
7 Guo J., Yang Y., Raghothamachar B., Kim T., Dudley M., Kim J. (2017) Understanding the microstructures of triangular defects in 4H-SiC homoepitaxial, *J. Crystal Growth* **480**, 119–125.
8 Kim H.-K., Kim S.I., Kim S., Lee N.-S., Shin H.-K., Lee C.W. (2020) Relation between work function and structural properties of triangular defects in 4H-SiC epitaxial layer: Kelvin probe force microscopic and spectroscopic analyses, *Nanoscale* **12**, 15, 8216–8229.
9 Abou-Ras D., Caballero R., Fischer C.-H., Kaufmann C., Lauermann I., Mainz R., Mönig H., Schöpke A., Stephan C., Streeck C., Schorr S., Eicke A., Döbeli M., Gade B., Hinrichs J., Nunney T., Dijkstra H., Hoffmann V., Klemm D., Efimova V., Bergmaier A., Dollinger G., Wirth T., Unger W., Rockett A., Perez-Rodriguez A., Alvarez-Garcia J., Izquierdo-Roca V., Schmid T., Choi P.-P., Müller M., Bertram F., Christen J., Khatri H., Collins R., Marsillac S., Kötschau I. (2011) Comprehensive comparison of various techniques for the analysis of elemental distributions in thin films, *Microsc. Microanal.* **17**, 5, 728–751.
10 Fujiwara H. (2007) *Spectroscopic ellipsometry: principles and applications*, Wiley.
11 Azzam R.M.A., Bashara N.M. (1987) *Ellipsometry and polarized light*, Elsevier Science Publishing Co, North-Holland.
12 Rosu D.-M., Ortel E., Hodoroaba V.-D., Kraehnert R., Hertwig A. (2017) Ellipsometric porosimetry on pore-controlled TiO_2 layers, *Appl. Surface Sci.* **421**, 487–493.
13 Sachse R., Moor M., Kraehnert R., Hodoroaba V.-D., Hertwig A. (2022) Ellipsometry-based approach for the characterization of mesoporous thin films for H_2 technologies, *Adv. Eng. Mater.* **24**, 6, 2101320.
14 Funke S., Miller B., Parzinger E., Thiesen P., Holleitner A.W., Wurstbauer U. (2016) Imaging spectroscopic ellipsometry of MoS_2, *J. Phys. Condens. Matter* **28**, 38, 385301.
15 Wurstbauer U., Röling C., Wurstbauer U., Wegscheider W., Vaupel M., Thiesen P.H., Weiss D. (2010) Imaging ellipsometry of graphene, *Appl. Phys. Lett.* **97**, 23, 231901.
16 Braeuninger-Weimer P., Funke S., Wang R., Thiesen P., Tasche D., Viöl W., Hofmann S. (2018) Fast, noncontact, wafer-scale, atomic layer resolved imaging of two-dimensional materials by ellipsometric contrast micrography, *ACS Nano* **12**, 8, 8555–8563.
17 Zollner S., Chen J.G., Duda E., Wetteroth T., Wilson S.R., Hilfiker J.N. (1999) Dielectric functions of bulk 4H and 6H SiC and spectroscopic ellipsometry studies of thin SiC films on Si, *J. Appl. Phys.* **85**, 12, 8353–8361.
18 Tiwald T.E., Woollam J.A., Zollner S., Christiansen J., Gregory R.B., Wetteroth T., Wilson S.R., Powell A.R. (1999) Carrier concentration and lattice absorption in bulk and epitaxial silicon carbide determined using infrared ellipsometry, *Phys. Rev. B* **60**, 16, 11464–11474.
19 Li H., Cui C., Bian S., Lu J., Xu X., Arteaga O. (2020) Double-sided and single-sided polished 6H-SiC wafers with subsurface damage layer studied by Mueller matrix ellipsometry, *J. Appl. Phys.* **128**, 23, 235304.
20 Synowicki R.A. (2008) Suppression of backside reflections from transparent substrates, *Phys. Status Solidi C* **5**, 5, 1085–1088.

21 Malacara D. (2007) *Optical shop testing*, Wiley.
22 De Groot P. (2015) Principles of interference microscopy for the measurement of surface topography, *Adv. Opt. Photonics* **7**, 1–65.
23 De Groot P.J. (2017) The meaning and measure of vertical resolution in optical surface topography measurement, *Appl. Sci.* **7**, 1, 54.
24 DIN ISO/IEC 17025:2017 (2017) *General requirements for the competence of testing and callibration laboratories.*